Journal of Materials Chemistry A

ROYAL SOCIETY OF CHEMISTRY

PAPER

View Article Online
View Journal | View Issue

Cite this: J. Mater. Chem. A, 2025, 13, 23073

Structural chemistry of the $n = 3$ Dion–Jacobson phases: controlling polarity and band gap†

Areesha Ali,[a] Vanessa Cascos,[b] Faith G. Pritchard,[c] Jan R. R. Verlet,[c] Nicole R. Sutherland,[a] Jack Woolley,[d] James Lloyd-Hughes,[d] Maxim Avdeev,[ef] Andy Beeby,[c] Stewart J. Clark[a] and Emma E. McCabe *[a]

Received 1st April 2025
Accepted 8th June 2025

DOI: 10.1039/d5ta02587g

rsc.li/materials-a

The Dion–Jacobson phases are increasingly gaining attention for their photoactivity and potential applications as photocatalysts and sensors, in addition to their polar structures. The structure – composition – property relationships for the $n = 3$ phases (of general formula $A'A_2B_3O_{10}$ *e.g.*, A' = Rb, Cs; A = Ca, Sr, Ba; B = Nb, Ta) are not well understood because of the lack of reliable structural models for this series. Our combined experimental and computational study addresses this by determining and explaining the complex structural chemistry of these materials, and provides a guide to allow structures and properties of new materials to be predicted and understood. We find that both A' and A cations determine the tilts of BO_6 octahedra and hence small A^{2+} ions tend to give materials with larger band gaps. The polar structures observed for A = Ca phases result from "proper" mechanisms and the role of the second-order Jahn–Teller effect of the B = Nb, Ta cations is discussed.

1. Introduction

Advancing photoactive materials for catalysis and optoelectronic applications requires a deep understanding of their electronic structure (band gaps, edge positions, and density of states), and the ability to strategically tune these properties through structural and compositional engineering. Mastering this control unlocks new possibilities for high-performance materials and transformative technologies. Layered perovskite-related materials including the Dion–Jacobson (DJ) phases have attracted attention due to their promise as photocatalysts,[1–6] photovoltaics[7–9] and X-ray- and photo-detectors.[10,11] DJ phases have significant compositional flexibility, attracting interest for a range of properties (including ionic conductivity[12] and ferroelectricity,[13–15] in addition to their photoactivity), and giving them huge potential to use composition to tune properties. However, efforts to design DJ materials optimised to specific applications are hampered by the lack of a full understanding of the structure–composition–property relationships in these materials.

The Dion–Jacobson phases (of general formula $A'A_{n-1}B_2O_{3n+1}$) adopt layered, pseudo-tetragonal crystal structures composed of perovskite blocks n layers thick, separated by A' cation layers (Fig. 1). As in other families of layered perovskites such as the Aurivillius phases, the B cations are often d^0 ions (such as Ti^{4+}, Nb^{5+}, Ta^{5+} ions) and are located in six-coordinate octahedral sites, whilst the larger A cations (*e.g.*, group 2 or lanthanide ions) are in 12-coordinate sites. The A' cations in DJ phases are typically much larger (*e.g.* group 1 ions such as Cs^+, Rb^+ in inorganic systems, or long "spacer" molecular ions in hybrid systems)[16] in more weakly-bound eight-coordinate sites (Fig. 1). The parent structure is tetragonal (of $P4/mmm$ symmetry)[17,18] and much analysis (both experimental and computational) is carried out assuming this ideal high symmetry (centrosymmetric) structure,[1,3,19] in part due to the difficulty of detecting distortions primarily involving light oxide ions by X-ray diffraction. However, the crystal structures of DJ phases can be tuned by changing their composition, taking advantage of both electronic and geometric factors.[20] As for other perovskite families, the DJ phases are susceptible to structural distortions involving rotations of the BO_6 octahedra about both in-plane and out-of-plane axes, and to in-plane polar and antipolar displacements.[13,20–22] These distortions have been explored for the $n = 2$ systems both experimentally and in computational studies,[13,22,23] but there has not yet been a systematic investigation of these distortions for the triple-layer phases, despite their importance as functional materials,[3,4,12] making it hard to predict structures and therefore properties. Building on earlier symmetry analysis of the tilts of BO_6 octahedra in $n = 3$ DJ phases,[20,21,24] in this combined

[a]Department of Physics, Durham University, South Road, Durham, DH1 3LE, UK. E-mail: emma.mccabe@durham.ac.uk
[b]CIEMAT, Department of Energy, Av. Complutense 40, Madrid, 28040, Spain
[c]Department of Chemistry, Durham University, South Road, Durham, DH1 3LE, UK
[d]Department of Physics, University of Warwick, Coventry, CV4 7AL, UK
[e]Australian Nuclear Science and Technology Organisation, New Illawarra Road, Lucas Heights, NSW, 2234, Australia
[f]School of Chemistry, The University of Sydney, Sydney, NSW, 2006, Australia

† Electronic supplementary information (ESI) available. See DOI: https://doi.org/10.1039/d5ta02587g

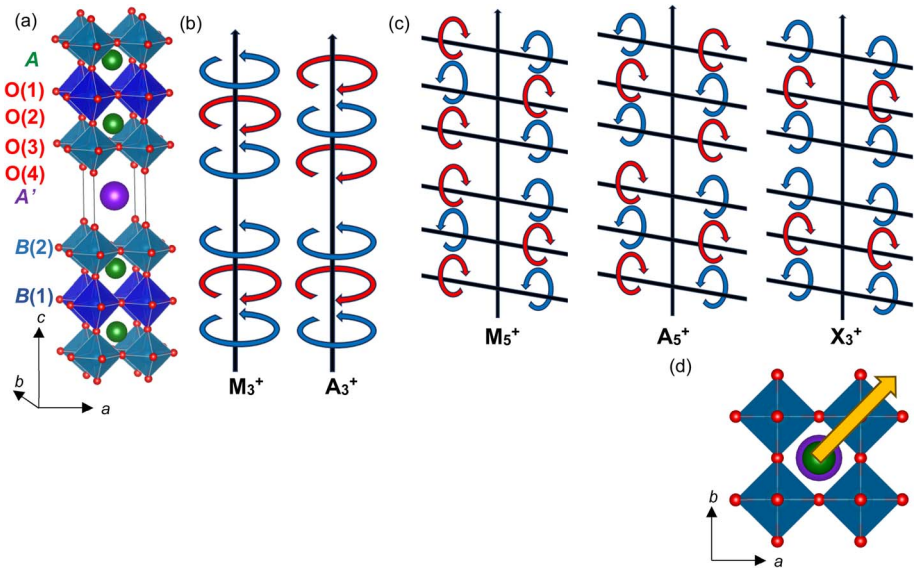

Fig. 1 (a) Shows the aristotype *P4/mmm* structure for an $n = 3$ DJ phase; (b) illustrates M_3^+ and A_3^+ rotations about the out-of-plane axis; (c) illustrates M_5^+, A_5^+ and X_3^+ rotations about in-plane axes, (curly red/blue arrows indicate directions of rotation of BO_6 octahedra); (d) illustrates in-plane polar displacements described by the Γ_5^- irrep along [110] of the *P4/mmm* unit cell, indicated by yellow arrow.

experimental and computational study we use second-harmonic generation and neutron powder diffraction to determine the crystal structures for some $A'A_2B_3O_{10}$ (A' = Rb, Cs; A = Ca, Sr, Ba; B = Nb, Ta) $n = 3$ DJ phases. We find that the A cation size plays a significant role (related to the perovskite tolerance factor)[25] in inducing tilts of BO_6 octahedra, but the nature of these tilts is also influenced by A' cation size. Comparison of Nb^{5+} and Ta^{5+} phases gives an indication of the balance between geometric and electronic factors in stabilising lower-symmetry structures. Our density functional theory (DFT) calculations are consistent with our experimental results and give an indication of the relative energies of these distortions. We show how this understanding of the structures (and in particular, the magnitude of BO_6 tilts) explains trends in band gap observed experimentally (in our work and previously reported[5,26]), and our understanding of polarity may be useful for designing optimised photoactive materials.

2. Methods

Polycrystalline powders of $CsA_2Nb_3O_{10}$ (A = Ba, Sr, Ca) and $CsCa_2Ta_3O_{10}$ were prepared by solid–state reaction. Stoichiometric amounts of Cs_2CO_3 (in 30% excess to account for volatility), $BaCO_3$, $SrCO_3$, $CaCO_3$, Nb_2O_5 and Ta_2O_5 were thoroughly ground in an agate mortar with acetone and the mixture was pressed into 10 mm diameter pellets. The resulting pellets were placed in an alumina crucible and heated at 550 °C for 12 h. A subsequent heating in air at 1000 °C for 12 h for $CsA_2Nb_3O_{10}$ (A = Sr, Ca) and for $CsCa_2Ta_3O_{10}$, or 850 °C for 3 h (A = Ba) was carried out. $RbA_2Nb_3O_{10}$ (A = Sr, Ca) were prepared similarly using 30% excess of Rb_2CO_3 with heating at 550 °C for 12 h followed by grinding and reheating at 1000 °C for 12 h. The initial characterization of the samples was carried out by laboratory X-ray powder diffraction (XRD) using a Rigaku Miniflex utilising Cu Kα radiation (40 kV, 15 mA) and a D/teX Ultra detector.

Neutron powder diffraction (NPD) data were collected at room temperature at the Echidna High Resolution Powder Diffractometer[27] in the Australian Centre for Neutron Scattering (ACNS), with $\lambda = 2.4395$ Å and at 1.6215 Å within the 2θ range from 10 to 165°. About 3 g of sample was contained in a vanadium can and data were collected for ~two hours per scan. Rietveld refinements[28] were carried out using the TopasAcademic software.[29] A scale factor and background terms were refined, followed by sample zero point and unit cell parameters. One or more profile parameters to describe the diffraction peak shape were refined, alongside the atomic coordinates for the strongest scattering site (as allowed by symmetry). More atomic coordinates were refined (as allowed by symmetry) as well as remaining profile parameters (assuming a pseudo-Voight peak shape) for stable refinements. Finally, atomic displacement parameters were refined in the final stages of the refinements. ISODISTORT was used for symmetry analysis (including exploring group–subgroup relations) and to describe distorted structures in terms of the parent structure with symmetry-adapted distortion modes applied.[24,30]

Diffuse reflectance spectra were recorded by grinding each sample with dry NaCl (10% w/w) and placing these mixtures in optical cuvettes and illuminating with a deuterium lamp (OceanOptics DH-2000-S). Non-specular scattered light was collected and the spectrum recorded using an OceanOptics spectrometer (Mayer2000 Pro). A cuvette of ground NaCl was used as a reference. The data were used to calculate the reflectance spectra $R(I)$ and Kubelka–Munk spectra $F(R)$.[31]

Preliminary second harmonic generation (SHG) measurements were carried out at University of Warwick. Hand-ground powders of each sample (of a wide range of particle sizes) were sealed between glass microscope slides and irradiated with an

800 nm laser and the SHG signal (400 nm) was detected using a photomultiplier tube (PMT), with filters to remove the fundamental. Using the Kurz and Perry powder technique,[32] further SHG measurements were carried out in Durham using powders of each sample that were sieved into different particle sizes and then placed into (GPE Secure 55) NMR tubes. While SHG is highly symmetry-dependent, the I_{SHG} efficiency of powders also depends on the particle size and if the particle size is not optimised, a false-negative result may be obtained. Powders were ground into bands of 38–45, 53–65, 65–75, 75–90 & 90–106 μm. A pulsed carbide laser generates the 1028 nm fundamental light at a rate of 150 Hz, with a pulse width of ~250 fs and this was used to irradiate the samples. The laser (0.2–9.5 mW) passed through a dichroic mirror and was then loosely focused on the sample using a parabolic mirror. The reflected second harmonic light (514 nm) was (again, loosely) collimated by the parabolic mirror, then reflected by the dichroic mirror back to a convex lens and focused to a system of filters to separate out remaining 1028 nm light. An amplified (10 dB) photodiode was used initially to establish SHG activity for each sample relative to a potassium dihydrogen phosphate (KDP) reference, as photodiodes have a large linear dynamic range. A photomultiplier tube (PMT) was used (due to its better sensitivity) to characterise the quadratic relationship between I_{SHG} and laser power for each sample, which confirms that the detected signal was due to a two-photon process. The signal was monitored on an oscilloscope. SHG efficiency below 0.5% KDP are generally characteristic of centrosymmetric materials with quadrupolar interactions, and so this is used as a threshold to avoid false-positive conclusions.[32]

Electronic structure calculations were performed within the *ab initio* density functional, plane-wave, pseudo-potential formalism as implemented in the Castep code.[33] The electronic wave functions are expanded in a plane wave basis set up to a kinetic energy cut off of ≥1000 eV. Integrations of the Brillouin zone were done with a *k*-point sampling scheme where the *k*-points are spaced at 0.05 $Å^{-1}$. We find this converges total energy differences to greater than 0.5 meV per atom. Our standard DFT calculations use the PBE exchange–correlation functional,[34] chosen for its balance between accuracy and computational efficiency making it a widely used choice for DFT calculations. Electron–ion interactions are described using *ab initio* ultra-soft pseudopotentials based on Vanderbilt's formalism[35] also generated with the PBE functional for consistency. The pseudo-potentials treat some of the semicore states as valence, which is important to obtain accurate electronic structures. In particular, this includes the 5s, 5p and 6s states for Cs; the 4s, 4p and 5s states for Rb; the 3s, 3p and 4s states for Ca; the 4s, 4p and 5s states for Sr; the 5s, 5p and 6s states for Ba; the 4s, 4p, 4d and 5s states for Nb; the 4f, 5s, 5p, 5d and 6s states for Ta, and the 2s and 2p states for O.

3. Results & discussion

3.1 Second harmonic generation tests for $A'A_2B_3O_{10}$

Preliminary SHG measurements carried out on hand-ground powder samples containing particles of a range of sizes which suggested some SHG activity for $CsCa_2B_3O_{10}$ (B = Nb, Ta) samples (see ESI†). Where I_{SHG} is not tested over multiple particle sizes, only a positive result is conclusive, so the samples were investigated further. Different particle size ranges were tested for the optimum efficiency, and the optimum available particle size for each sample was then used to qualify samples as SHG active (resulting from a non-centrosymmetric structure). The threshold chosen was <0.5% KDP, below which is considered a negative result.[36–38] This is in line with contributions from quadrupolar effects or surface contributions measured in related perovskite materials,[38] more general estimates of the surface contribution,[37] and our own measurements of centrosymmetric NaCl powder (Fig. 2). The photodiode-measured SHG response to a KDP reference is shown in Fig. 2a (left hand axis). On the right axis, the SHG response measured for $CsA_2B_3O_{10}$ (A = Ca, Sr, Ba; B = Nb, Ta) samples is shown. All samples showed a quadratic relationship with laser power, suggesting the detected light arose from a two-photon process. I_{SHG} measurements using a PMT (Fig. 2b) revealed moderate SHG activity (>1% that of KDP) for $CsCa_2Nb_3O_{10}$ and for $RbCa_2Nb_3O_{10}$, weak SHG activity (>0.5% that of KDP) for $CsCa_2Ta_3O_{10}$ and negligible SHG activity (comparable to NaCl powder) for <45 μm $CsSr_2Nb_3O_{10}$, $RbSr_2Nb_3O_{10}$ and $CsBa_2Nb_3O_{10}$ (though it was not possible to do a full particle size study for these samples).

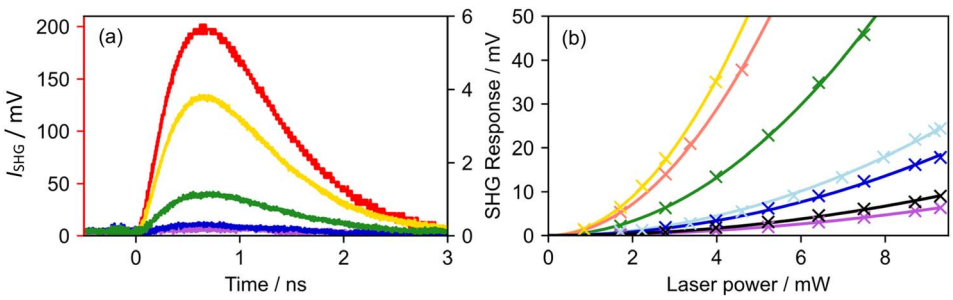

Fig. 2 HG measurements showing (a) the response of a photodiode to the SH from KDP (75–90 μm particles; red, left red axis), $CsCa_2Nb_3O_{10}$ (<45 μm particles; yellow, right axis), $CsCa_2Ta_3O_{10}$ (45–53 μm particles; green, right axis), $CsBa_2Nb_3O_{10}$ (<45 μm particles; purple, right axis); (b) shows the SHG intensity I_{SHG} as a function of laser power measured by a PMT (showing quadratic dependence) for $CsCa_2Nb_3O_{10}$ (yellow, 45–53 μm), $CsCa_2Ta_3O_{10}$ (green, 90–106 μm), $RbCa_2Nb_3O_{10}$ (salmon, 76–90 μm), NaCl (light blue, 90–106 μm), $CsSr_2Nb_3O_{10}$ (blue, <45, unoptimized), $RbSr_2Nb_3O_{10}$ (black, <45 μm, unoptimized) and $CsBa_2Nb_3O_{10}$ (purple, <45 μm, unoptimised).

3.2 Structure refinements for $A'A_2B_3O_{10}$

3.2.1 Symmetry analysis for $A'A_2B_3O_{10}$. Before exploring the structural chemistry of these $A'A_2B_3O_{10}$ phases in detail, it's useful to summarise the key structural distortions expected for these $n = 3$ DJ phases. As shown in Fig. 1, the ideal aristotype structure of *P*4/*mmm* symmetry has a single *A* cation site and two *B* sites: the higher symmetry *B*(1) in the centre of the perovskite blocks, and the lower symmetry *B*(2) site in the outer layers of the blocks. As in many layered perovskite-related phases, the *B*(2) ions tend to be displaced along the long (pseudo-) tetragonal axis of the unit cell towards the *A*′ layers. This lowers the *B*(2) site symmetry to C_{4v}. Distortions that lower the unit cell symmetry from *P*4/*mmm* include:

• Rotations of BO_6 octahedra about the long axis (Fig. 1b):

- Rotations in adjacent blocks in-phase with one another; described by M_3^+ irrep ($k = \frac{1}{2}\frac{1}{2}0$); symmetry lowered to *P*4/*mbm* (note that rotations of $B(1)O_6$ and $B(2)O_6$ octahedra within each block are not constrained to be either in-phase or out-of-phase), Fig. 1b;

- Rotations in adjacent blocks out-of-phase with one another; described by A_3^+ irrep ($k = \frac{1}{2}\frac{1}{2}0$); symmetry lowered to *I*4/*mcm* (note that rotations of $B(1)O_6$ and $B(2)O_6$ octahedra within each block are not constrained to be either in-phase or out-of-phase), Fig. 1b;

• Rotations of BO_6 octahedra about in-plane axes (Fig. 1c):

- Out-of-phase tilts with tilts in adjacent blocks in-phase with one-another ($(a^-a^-c^0)$ $(a^-a^-c^0)$); described by M_5^+ irrep ($k = \frac{1}{2}\frac{1}{2}0$); symmetry lowered to *Pbmn* (*cab* setting of space group 53, *Pmna*), Fig. 1c;

- Out-of-phase tilts with tilts in adjacent blocks out-of-phase with one-another ($(a^-a^-c^0)$–$(a^-a^-c^0)$); described by A_5^+ irrep ($k = \frac{1}{2}\frac{1}{2}\frac{1}{2}$); symmetry lowered to *Icmm* ($\bar{c}ba$ setting of space group 74, *Imma*), Fig. 1c;

- In-phase tilts with tilts in adjacent blocks in-phase with one-another ($(a^+b^+c^0)$ $(a^+b^+c^0)$); described by X_3^+ irrep ($k = 0\frac{1}{2}0$); symmetry lowered to *Pmmn*, Fig. 1c;

• In-plane polar displacements (Fig. 1d):

- Polar displacement along [110] direction of the parent *P*4/*mmm* unit cell; described by Γ_5^- irrep ($k = 0\ 0\ 0$); symmetry lowered to *C*2*mm* ($\bar{c}ba$ setting of space group 38, *Amm*2), Fig. 1d;

As indicated in Fig. 1, we can expect that structural distortions in these DJ phases primarily involve shifts in the oxide positions. However these are very hard (or even impossible) to detect using X-ray powder diffraction (XRPD) for which the scattering of light oxide ions is very weak compared with that of the heavier Rb, Cs, Nb and Ta ions which will dominate the X-ray scattering. XRPD is perhaps the most accessible technique for routine structural characterisation of samples and so most of the phases reported in our study (and closely-related materials) have been reported to adopt the ideal aristotype *P*4/*mmm* structure.[6,39–42]

An early single crystal X-ray diffraction study on $CsCa_2Nb_3O_{10}$ indicated a large orthorhombic cell and reported a structure[18] very similar to ours determined from NPD analysis (Section 3.2.4), highlighting the advantages of single crystal diffraction over powder, if suitable single crystals are available. A combined computational and experimental study using ssNMR on $RbSr_2Nb_3O_{10}$ indicated the *P*4/*mbm* model (consistent with ours, Section 3.2.6)[43] but there has not been a wider consideration of these structures and the distortions observed to identify structural trends within this family. More recent studies have included phases with smaller *A* cations as well as ns^2 cations and give glimpses of the complex structural chemistry of the $n = 3$ DJ phases.[26,42,44,45] This has motivated our study to explore the structural chemistry of these materials, to understand how it relates to their physical properties, and to identify structural trends to allow structures and therefore properties of $n = 3$ DJ phases to be predicted.

3.2.2 Structure refinement for $CsBa_2Nb_3O_{10}$. In the combined analysis, the 2.44 Å and 1.62 Å room temperature NPD data for $CsBa_2Nb_3O_{10}$ were fitted well by the aristotype structure of *P*4/*mmm* symmetry (Fig. 1), although traces of $Ba_3Nb_5O_{15}$ (9.8(4)% by mass) are thought to contribute to a peak at 2.11 Å (~45° 2θ) in the 1.62 Å data set (a further small peak at ~0.9 Å (~125° 2θ) in the 1.62 Å data was observed and could not be fitted by possible impurity phases or lower symmetry models). This refined model (Fig. 1 and ESI†) is in agreement with that reported by Weppner *et al.* from analysis of XRPD data.[41] Lower symmetry models that would allow rotations of the NbO_6 octahedra or polar displacements did not give significant improvements in fit and so the average structure of $CsBa_2Nb_3O_{10}$ (with tolerance factor of the hypothetical "$BaNbO_3$" blocks of 1.05) seems to be best described by the high symmetry *P*4/*mmm* model with no rotations of octahedra. However we cannot rule out that such distortions may occur at a more local length-scale, which may give more optimal coordination environments for several sites.

NPD data for all other phases considered here could not be fitted satisfactorily by the high symmetry *P*4/*mmm* model: extra peaks were observed in NPD data indicating larger unit cells, and/or intensities were not well fitted and the models were unphysical (with very distorted polyhedral, and unphysical atomic displacement parameters). This highlights the challenges of structural characterisation using XRPD data[40–42] for these perovskite-related materials for which many distortions involve displacements of the light oxide ions (which give relatively weaker scattering of X-rays compared with the heavier cations present). Lower symmetry models allowing rotations of BO_6 octahedra were therefore considered to fit our NPD data for all other samples.

3.2.3 Structure refinement for $CsSr_2Nb_3O_{10}$. Attempts to fit the room temperature NPD data for $CsSr_2Nb_3O_{10}$ by the aristotype *P*4/*mmm* model (as reported by Weppner *et al.* from XRPD data)[41] weren't successful: there was a significant mismatch between observed and calculated intensities (see ESI†) and an unfeasibly high atomic displacement parameter for O(1) ($U_{iso} \times 100 = 8.5(2)$ Å^2 for the equatorial site at the centre of the perovskite layers). Allowing this to refine anisotropically suggested significant displacement of O(1) away from the ideal 2*f* site, consistent with rotation of the NbO_6 octahedra about $[001]_t$. This prompted us to consider models that allowed rotation of the octahedra about the out-of-plane axis and the fit improved significantly for the *P*4/*mbm* model (M_3^+) (see ESI†). A

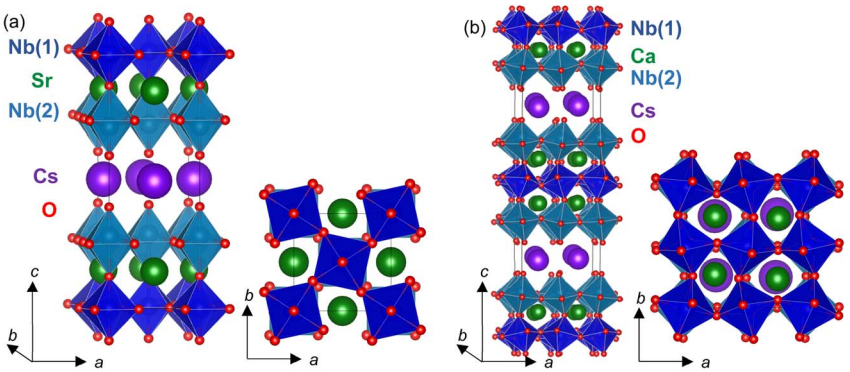

Fig. 3 (a) Refined $P4/mbm$ (M_3^+) structure for $CsSr_2Nb_3O_{10}$ and (b) refined $P2_1cn$ ($A_5^+ + X_3^+ (+M_3^+) + \Gamma_5^-$) model for $CsCa_2Nb_3O_{10}$, with Nb(1)O_6 and Nb(2)O_6 octahedra in dark and light blue, Cs^+, (Sr, Ca)$^{2+}$ and O^{2-} ions in purple, green and red, respectively.

non-centrosymmetric model of $P2_1am$ symmetry was also considered but gave negligible improvement in fit (see ESI†). This suggests that the average structure is best described by a non-polar model $P4/mbm$ symmetry (ESI† and Fig. 3), consistent with the negligible SHG activity (see Section 3.1). However, as noted above for $CsBa_2Nb_3O_{10}$, we cannot rule out the possibility that additional distortions (such as rotations of octahedra, or polar displacements) may occur at a more local length-scale in order to give more optimal coordination environments for several sites *e.g.* Sr site which is noticeably over-bonded in the $P4/mbm$ model (Table S14†).

Although the hypothetical "$SrNbO_3$" perovskite blocks in $CsSr_2Nb_3O_{10}$ again have tolerance factor close to 1 ($t = 0.99$), the decrease as Ba^{2+} is replaced by smaller Sr^{2+} (12-coordinate ionic radii of 1.44 Å and 1.61 Å for Sr^{2+} and Ba^{2+}, respectively)[46] is sufficient to stabilise rotations of the NbO_6 octahedra about this out-of-plane axis. Presumably this occurs to optimise bonding within the perovskite layers, and it results in a significant reduction of the in-plane unit cell parameter (3.97705(5) Å for $CsBa_2Nb_3O_{10}$ compared with 3.90786(6) Å for $CsSr_2Nb_3O_{10}$ (normalised by dividing by $\sqrt{2}$ for comparison with the $P4/mmm$ model)).

3.2.4 Structure refinement for $CsCa_2Nb_3O_{10}$. Attempts to fit the room temperature NPD data for $CsCa_2Nb_3O_{10}$ using the parent structure were not successful with unindexed peaks and significant mismatch in intensities (see ESI†). Allowing high atomic displacement parameters to refine anisotropically gave anisotropic values consistent with rotation of NbO_6 octahedra about the out-of-plane axis. This led us to consider lower symmetry models to allow these rotations. Refinements using the $P4/mbm$ (M_3^+ rotations) model gave improved fits but some peaks were not well-matched (see ESI†), and atomic displacement parameters for the apical oxide sites refined to high values (and anisotropic refinements suggested displacements in the ab plane). These results prompted us to consider models allowing additional rotations of NbO_6 octahedra about an in-plane axis. A mode inclusion analysis[47] was carried out (see ESI†), to identify which group of displacive modes (in addition to the M_3^+ rotations) would give the biggest improvement in fit (assuming a lower symmetry unit cell up to $2a_t \times 2a_t \times 2c_t$). This indicated that the fit improved significantly if A_5^+ or X_3^+ distortions (which both describe rotations of NbO_6 octahedra about an in-plane axis) were included (see ESI†). Combining A_5^+ rotations with the X_3^+ ($+M_3^+$) rotations gives a large unit cell of $Pnma$ symmetry ($2c_t \times 2a_t \times 2a_t$). This model gave a good fit to the data and is consistent with that reported from single crystal X-ray diffraction for $CsCa_2Nb_3O_{10}$ (reported as 30.185(3) Å × 7.740(2) Å × 7.746(2) Å in space group $Pnam$ ($ac\bar{b}$ setting of space group 62),[18] and so is equivalent to our model in the standard setting, $Pnma$).[18] Subsequently our $A_5^+ + X_3^+$ ($+M_3^+$) $Pnma$ model will be referred to in the non-standard $Pmcn$ (bca) setting (to give the long axis along c) for ease of comparison with other structural models. The atomic displacement parameters for sites derived from the same site in the parent $P4/mmm$ structure were constrained to be equal, given the large unit cell which is pseudo-tetragonal. This model allows a complex modulation of NbO_6 rotations and gives lower symmetry sites for A^{2+} cations (four 4c sites of m symmetry in this $Pmcn$ model, compared with the single 4f site of $2mm$ symmetry for the $P4/mbm$ model described above for $CsSr_2Nb_3O_{10}$). This complex structure presumably results from the lower tolerance factor ($t = 0.96$) for the "$CaNbO_3$" blocks with more significant tilts needed to optimise bonding around the smaller Ca^{2+} ion. It is striking that the earlier structural study by Dion *et al.* using single crystal X-ray diffraction[18] is in good agreement with our study using NPD data, in contrast with other studies on related materials using X-ray powder diffraction data, highlighting the advantages of single crystal X-ray diffraction compared with XRPD for these systems.

Given the significant SHG response for this sample (Section 3.1), polar models of $Pna2_1$ and $Pmn2_1$ symmetries were considered. These models allow the same tilts as the $Pmcn$ model as well an in-plane polarisation (described by the Γ_5^- irrep) along different in-plane directions (see ESI†). It is hard to confirm either of these polar $Pna2_1$ and $Pmn2_1$ models from analysis of our diffraction data: the improvement in fit over the $Pmcn$ model was not visible but was noticeable in the fitting statistics for both models. Full details are given in the ESI† and the $Pna2_1$ model is illustrated in Fig. 3. Again for ease of comparison between models, the cba setting, $P2_1cn$, of space group 33 $Pna2_1$ will be used (with polar axis along a and long axis along c), and the cab setting, $P2_1mn$, of space group 31

$Pmn2_1$ will be used (with polar axis along a and long axis along c).

3.2.5 Structure refinement for $CsCa_2Ta_3O_{10}$. To investigate the role of the SOJT effect for the transition metal B cations, the Ta analogue $CsCa_2Ta_3O_{10}$ was investigated. As for $CsCa_2Nb_3O_{10}$, additional peaks were observed that could not be indexed by the $P4/mmm$ unit cell suggested from previous work using XRPD,[42] and atomic displacement parameters suggested some rotations of TaO_6 octahedra about both in-plane and out-of-plane axes. As for $CsCa_2Nb_3O_{10}$, mode inclusion analysis indicated that the fit was most improved by allowing rotations about an in-pane axis (either X_3^+ or A_5^+ tilts), but models allowing these modes alone did not index all reflections. Again the $A_5^+ + X_3^+$ ($+M_3^+$) $Pmcn$ model described above for $CsCa_2Nb_3O_{10}$ gave a good fit to the data. Given the weak SHG activity, polar models of $P2_1cn$ and $P2_1mn$ symmetries were also considered, as for $CsCa_2Nb_3O_{10}$. Again these models gave similar fits and it is hard to distinguish between them and both models include some sites for which bond valence sum values are not ideal. These likely suggest some deficiencies in our models: these might arise from the complexity of the model and the fact that the unit cell is close to metrically tetragonal, giving rise to pseudo-symmetry issues. Full refinement details are given in the ESI.†

Two Rb analogues, $RbSr_2Nb_3O_{10}$ and $RbCa_2Nb_3O_{10}$, were also studied for comparison with the Cs phases to understand the role of the interlayer A' cations Cs^+ and Rb^+.

3.2.6 Structure refinement for $RbSr_2Nb_3O_{10}$. As for $CsSr_2Nb_3O_{10}$, attempts to fit the $RbSr_2Nb_3O_{10}$ NPD data by the ideal $P4/mmm$ model gave some mismatch of intensities and an unfeasibly high atomic displacement parameter ($U_{iso} \times 100 = 9.6(2)$ Å^2) for the equatorial oxide site O(1). Allowing this atomic displacement parameter to refine anisotropically suggested significant displacement of O(1) away from the ideal $2f$ site, consistent with rotation of the NbO_6 octahedra about $[001]_t$. Both $P4/mbm$ (M_3^+ rotations) and $I4/mcm$ (A_3^+ rotations) models gave significant improvements in fit (see ESI†), with the $P4/mbm$ (M_3^+) model being slightly better, as found above for $CsSr_2Nb_3O_{10}$. As for $CsSr_2Nb_3O_{10}$ discussed above, a polar $P2_1am$ model was also considered for $RbSr_2Nb_3O_{10}$ but gave negligible improvement in fit. These observations and the negligible SHG signal (see Section 3.1) suggest that the average structure, at least at the length scales probed by neutron diffraction, is best described by non-polar $P4/mbm$ symmetry. This is consistent with studies using NPD and Raman spectroscopy reported by Kurzman and Geselbracht.[48] Refinement details are given in the ESI† and the structure is illustrated in Fig. 4; the refined amplitude for the M_3^+ distortion mode was 0.64 Å.

3.2.7 Structure refinement for $RbCa_2Nb_3O_{10}$. As for $CsCa_2Nb_3O_{10}$ described above, additional peaks were observed in $RbCa_2Nb_3O_{10}$ NPD data that could not be fitted by the ideal $P4/mmm$ model, and this model also gave high atomic displacement parameters for equatorial O(1) site and apical O(2) site (when refined anisotropically, these suggested some rotation of NbO_6 octahedra about both the out-of-plane axis and an in-plane axis). Mode inclusion analysis suggested the greatest improvement in fit came from allowing X_3^+ rotations about an in-plane axis. Models allowing these X_3^+ rotations (including a $Pmma$ model ($2a_t \times a_t \times c_t$) and a $Pmmn$ model ($2a_t \times 2a_t \times c_t$)) gave some mismatched intensities, and fairly high atomic displacement parameters for some oxide sites (see ESI†). A second round of mode inclusion analysis suggested that also allowing M_5^+ rotations (again about an in-plane axis) would improve the fit further. Similar to $CsCa_2Nb_3O_{10}$, symmetry analysis indicates that X_3^+ tilts (with order parameter (a,b)) also allows M_3^+ rotations about the out-of-plane axis, and when M_5^+ tilts (about an in-plane axis) are also allowed, the symmetry is lowered to $P2_1/m$. This model gave a significant improvement in fit and refinement details are given in the ESI.† A $P2_1/m$ model has also been proposed for $RbCa_2Nb_3O_{10}$ by Kurzman and Geselbracht, but with the long axis doubled, although atomic coordinates are not given so it's hard to make a detailed comparison.[48]

Given the moderate SHG activity measured for $RbCa_2Nb_3O_{10}$ (Section 3.1), models allowing for an in-plane polar displacement (described by the Γ_5^- mode) were also considered. The polar $P2_1$ model gave a slight improvement in fit. Refinement details are given in the ESI† and the structure is illustrated in Fig. 4. We note that the polar displacement is relatively small (mode amplitudes of 0.53 Å, 0.77 Å, 0.64 Å and 0.26 Å for M_3^+, X_3^+, M_5^+ and Γ_5^- modes, respectively), comparable to that refined for $CsCa_2Nb_3O_{10}$. However, with a single set of NPD data for $RbCa_2Nb_3O_{10}$, the uncertainties in refined positions are nearly three times larger for $RbCa_2Nb_3O_{10}$ than for $CsCa_2Nb_3O_{10}$, and most sites for the Rb phase refine to positions close to

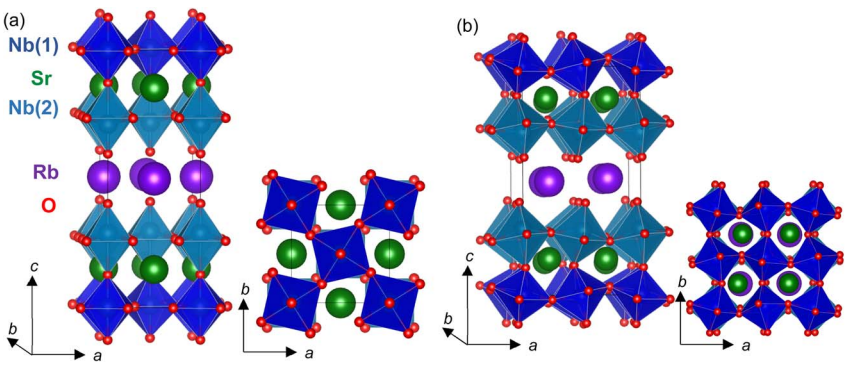

Fig. 4 (a) Refined $P4/mbm$ (M_3^+) structure for $RbSr_2Nb_3O_{10}$ and (b) refined $P2_1$ ($M_5^+ + X_3^+$ ($+M_3^+$) + Γ_5^-) model for $RbCa_2Nb_3O_{10}$, with Nb(1)O_6 and Nb(2)O_6 octahedra in dark and light blue, Rb^+, (Sr, Ca)$^{2+}$ and O^{2-} ions in purple, green and red, respectively.

within an uncertainty of the non-polar model, making it hard to confirm this polar distortion from analysis of our NPD data.

3.3 Diffuse reflectance measurements of optical band gap

Diffuse reflectance measurements for these $A'A_2B_3O_{10}$ phases showed a decrease in reflectance for $\lambda > 300$ nm. The diffuse reflectance spectra after the Kubelka–Munk treatment are shown in Fig. 5. The intercepts of the linear increase in Kubelka–Munk function $F = (1-R)^2/2R$ (where R is the diffuse reflectance) with the energy axis can be used to estimate the optical band gap, and suggest gaps ranging from 3.25 to 3.65 eV for $CsA_2Nb_3O_{10}$, with gap increasing with decreasing A cation size. Similar gaps were measured for $RbA_2Nb_3O_{10}$ samples. Data for $CsCa_2Ta_3O_{10}$ are very noisy but suggest a slightly larger gap than for $CsCa_2Nb_3O_{10}$, broadly consistent with the combined experimental and computational study by Zahedi *et al.*[1]

These results are consistent with the white-off-white colour of the samples, and bandgaps in the visible-UV region of the electromagnetic spectrum.[1,49] The low absorption observed for these materials is consistent with their indirect band gaps.[50]

3.4 Geometry optimisations from density functional theory calculations

Geometry optimisations of possible lower symmetry structures were carried out using DFT and the relative energies of distorted structures with respect to the ideal *P*4/*mmm* parent structure are summarised for several compositions in ESI† and Fig. 6. The first observation is that the structures calculated to be low in energy are in good agreement with those determined experimentally from NPD analysis (Section 3.2):

• For $CsBa_2Nb_3O_{10}$, only very small decreases in energy are calculated for possible distortions, consistent with the *P*4/*mmm* experimental model.

• For $CsSr_2Nb_3O_{10}$ the single irrep that gives the greatest decrease in energy is M_3^+ (tilts about the out-of-plane axis, in-phase between blocks), consistent with the *P*4/*mbm* experimental mode.

- M_3^+ and A_3^+ modes (tilts about the out-of-plane axis, in-phase between blocks and out-of-phase, respectively) give very similar energy decreases, reflecting the weak dispersion (and reduced connectivity between blocks) as reported for $CsLn_2Ti_2NbO_{10}$.[20]

- The X_3^+ tilts (tilts about an in-plane axis) combined with M_3^+ tilts give negligible stabilisation over the M_3^+-only *P*4/*mbm* model, and similarly M_5^+ and A_5^+ tilts (about in-plane axes) give negligible stabilisations.

• For $A'Ca_2B_3O_{10}$ (A' = Rb, Cs; B = Nb, Ta) the single irreps that give the greatest stabilisation are those that describe rotations about in-plane axes (M_5^+ for A' = Rb; A_5^+ for A' = Cs), in contrast to the Sr analogues. Tilts about the out-of-plane axis (A_3^+, M_3^+) also give some stabilisation.

- Combining the M_5^+ or A_5^+ mode with the X_3^+ mode (which also allows M_3^+ tilts) gives non-polar models of $P2_1/m$ symmetry ($RbCa_2Nb_3O_{10}$) or *Pmcn* symmetry ($CsCa_2B_3O_{10}$, B = Nb, Ta).

- For both $A'Ca_2Nb_3O_{10}$ (A' = Rb, Cs), there's a noticeable energy stabilisation by adding an additional in-plane polar distortion (Γ_5^-) to give polar models of $P2_1$ symmetry ($RbCa_2Nb_3O_{10}$, energy gain 5 meV per formula unit) or $P2_1cn$ symmetry ($CsCa_2Nb_3O_{10}$, energy gain ~12 meV per formula unit) compared with the non-polar $P2_1/m$ or *Pmcn* models, respectively. The amplitude of the polar distortion from DFT calculations is comparable for these two phases, and consistent with the moderate SHG activity measured for these phases (Section 3.1).

- In contrast, for $CsCa_2Ta_3O_{10}$ there's only a negligible energy decrease (0.2 meV per formula unit) by allowing this additional in-plane polar distortion, and the amplitude of the polar distortion in the DFT-optimised models is negligible. This is consistent with the very weak SHG activity measured for $CsCa_2Ta_3O_{10}$ (Section 3.1).

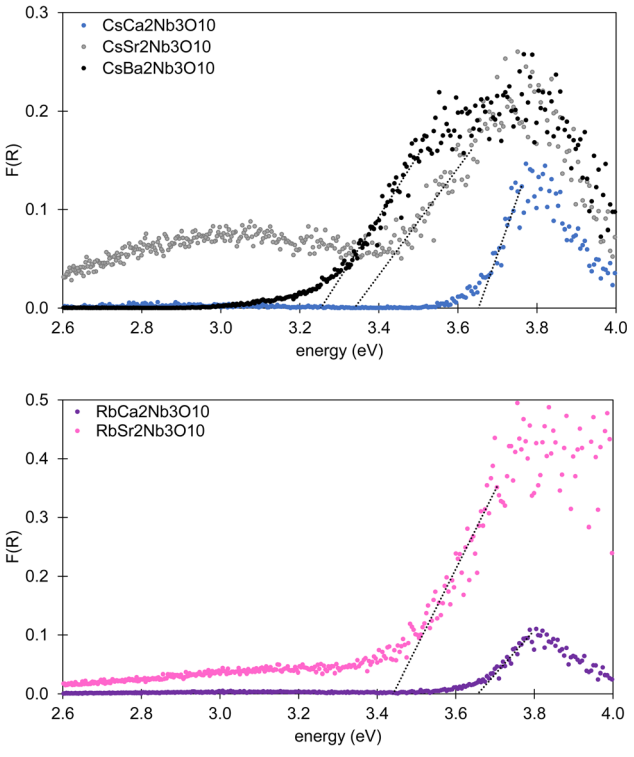

Fig. 5 Diffuse reflectance spectra collected for $A'A_2Nb_3O_{10}$ samples diluted in dry NaCl after Kubelka–Munk treatment showing bandgaps in the UV region; upper panel shows spectra for $CsCa_2Nb_3O_{10}$ (blue), $CsSr_2Nb_3O_{10}$ (grey) and $CsBa_2Nb_3O_{10}$ (black), and lower panel shows spectra for $RbCa_2Nb_3O_{10}$ (purple) and $RbSr_2Nb_3O_{10}$ (pink).

4. Discussion

Exploring trends in the experimentally refined structures gives a deeper understanding of the structural chemistry and physical properties of these systems. Fig. 7 summarises the unit cell parameters for these five compositions. As expected given their ionic radii (eight-coordinate radii are 1.61 Å and 1.74 Å for Rb and Cs, respectively),[46] the Rb phases are smaller than the Cs analogues. The long c parameter is much larger for the Cs phases whilst both series have very similar in-plane unit cell parameters, reflecting this in-plane direction being more constrained against compression by the widths of the perovskite

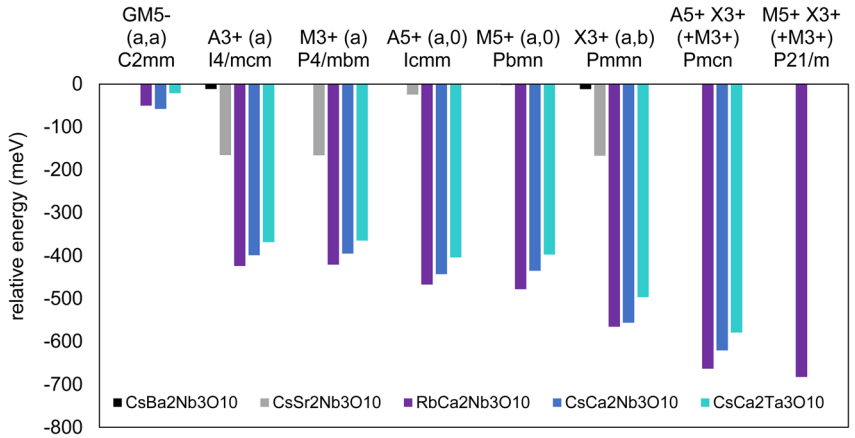

Fig. 6 Summary of the calculated energies of lower symmetry structures for several $A'A_2B_3O_{10}$ (A' = Rb, Cs; A = Ca, Sr, Ba; B = Nb, Ta) compositions relative to the ideal *P4/mmm* structures (energies were calculated per formula unit). Note that allowing additional an in-plane polar distortion to the *Pmcn* and $P2_1/m$ models to lower the symmetries to $P2_1cn$ and $P2_1$, respectively, gives further energy gains of ~12 eV and 0.2 eV for $CsCa_2Nb_3O_{10}$ and $CsCa_2Ta_3O_{10}$, respectively, and 5 eV for $RbCa_2Nb_3O_{10}$.

blocks. It is striking that the *c* parameter for $CsBa_2Nb_3O_{10}$ (with highest tolerance factor and no octahedral rotations) is smaller than expected compared with other phases, reflecting the reduced height of the CsO layers to give optimal Cs bonding when stacked with the wider (and untilted) "$BaNbO_3$" perovskite blocks.

The orthorhombic strain[51] (Fig. 7d) is calculated from the normalised in-plane unit cell parameters according to the eqn (1)

$$\text{Orthorhombic strain} = \left|\frac{a-b}{a+b}\right| \quad (1)$$

and $CsBa_2Nb_3O_{10}$, $CsSr_2Nb_3O_{10}$ and $RbSr_2Nb_3O_{10}$ (with no rotations of octahedra about an in-plane axis) remain tetragonal with zero orthorhombicity. $CsCa_2Nb_3O_{10}$, $CsCa_2Ta_3O_{10}$ and $RbCa_2Nb_3O_{10}$ all adopt orthorhombic or monoclinic structures with rotations of BO_6 octahedra about in-plane axes and to explore the different degrees of orthorhombicity for these three Ca phases (and in particular the origin of different behaviour for Nb and Ta analogues, given their identical ionic radii (six-coordinate radii of 0.64 Å)),[46] the rotations and cation displacements need to be considered. It is clear that the rotations of octahedra (and therefore the orthorhombic strain) are strongly influenced by the sizes of A^{2+} cations (12-coordinate

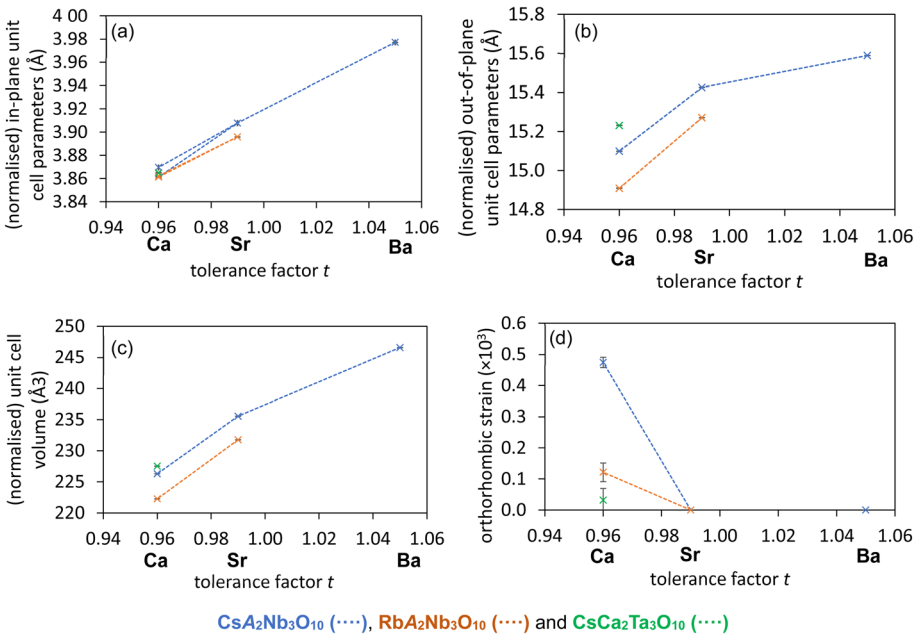

Fig. 7 Summary of key unit cell parameters (a–c) and orthorhombic strain (d) from refinements using room temperature NPD data for $CsA_2Nb_3O_{10}$ (blue), $RbA_2Nb_3O_{10}$ (orange) and $CsCa_2Ta_3O_{10}$ (green); A = Ca, Sr and Ba. Normalised values for unit cell parameters for models with larger unit cells are calculated for these plots to aid comparisons between models.

ionic radii of Ca^{2+}, Sr^{2+} and Ba^{2+} are 1.34 Å, 1.44 Å and 1.61 Å, respectively).[46]

We note that the structures suggested here for $CsCa_2B_3O_{10}$ (B = Nb, Ta) are challenging to refine experimentally because of their complexity (particularly for B = Ta with unit cell close to metrically tetragonal) leading to pseudo-symmetry issues and some correlation between refined parameters. The refined models include some irregular octahedra and large distributions of tilts and out-of-centre displacements (see uncertainties in ESI†) and these features are unlikely to give a good representation of the average structure. For comparison between B = Nb, Ta models, the geometry-optimised models from DFT calculations (assuming 0 K) might be more helpful for elucidating trends within this series.

The first observation across all of the lower-symmetry structural models is that the rotations of BO_6 octahedra about the long axis (the M_3^+ rotations) are much larger for the $B(1)O_6$ octahedra in the centre of the perovskite blocks, and are minimal (often negligible) for the $B(2)O_6$ octahedra in the outer layers of the octahedra (see refinement details in the ESI†). Overall, there's little change in the magnitude of these tilts across these $A'A_2B_3O_9$ (A' = Rb, Cs; A = Sr, Ca and B = Nb, Ta) compositions, suggesting that these tilts about the long axis occur to optimise bonding around the A cations. If these M_3^+ rotations occur to optimise A^{2+} bonding (*e.g.* to reduce Sr–O bond lengths for a given Nb–O bond length) there must be some maximum M_3^+ tilt angle, limited by the A' = Rb, Cs cation size, beyond which the in-plane unit cell parameters would decrease too much to avoid overbonding of the A' cations. This might explain the slightly larger M_3^+ tilts (particularly for the outer $Nb(2)O_6$ octahedra) for the Rb phases compared with their Cs analogues (see ESI†).

These M_3^+ tilts alone are therefore not sufficient to give good bonding about the smallest A = Ca cations and so additional tilts about in-plane axes are observed for $CsCa_2B_3O_{10}$ (B = Nb, Ta) and for $RbCa_2Nb_3O_{10}$. These are surprisingly complex, involving two tilt modes to give tilts of different magnitudes through the structure. The experimentally observed models are consistent with those expected from DFT calculations (see Fig. 6 and ESI†): considering single tilts, A_5^+ and M_5^+ tilts give the largest energy stabilisations for $CsCa_2B_3O_{10}$ and for $RbCa_2Nb_3O_{10}$, respectively. This can be understood in terms of the effect of these tilts on the coordination environments of the A' cations:

- A_5^+ tilts with $k = (\frac{1}{2}\,\frac{1}{2}\,\frac{1}{2})$ (to give a model of *Icmm* symmetry) rotate BO_6 octahedra about [110] of the parent structure, with tilts in successive perovskite blocks in opposite directions (Fig. 8). This results in the apical oxide sites above and below a given A' cation being displaced in the same direction. Presumably this becomes increasingly unfavourable with decreasing size of A'.
- M_5^+ tilts with $k = (\frac{1}{2}\,\frac{1}{2}\,0)$ (to give a model of *Pbmn* symmetry) again rotate BO_6 octahedra about [110] of the parent structure but in this case, the tilts in successive perovskite blocks are in the same directions, and so for these three-layer systems, M_5^+ tilts cause the apical oxide sites above and below an A' cation to be displaced in opposite directions, likely to be more electrostatically favourable as the A' cation (and therefore the distance between apical oxide sites across these layers) get smaller.

The same logic can be applied to the n = 2 DJ phases, noting that for these structures containing an even number of layers of octahedra in the perovskite blocks, the irreps are the other way around:

- A_5^- ($k = (\frac{1}{2}\,\frac{1}{2}\,\frac{1}{2})$) modes describe $(a^-a^-c^0)$–$(a^-a^-c^0)$ rotations with displacements of apical oxide sites above and below the A' layer in opposite directions, hence these tilts are favoured for A' = Rb;[15,22,52]
- M_5^- ($k = (\frac{1}{2}\,\frac{1}{2}\,0)$) modes describe $(a^-a^-c^0)$ $(a^-a^-c^0)$ rotations with displacements of apical oxide sites in the same direction, A' = Cs.[15,22,52]

The X_3^+ tilts are more unusual: with $k = (0\,\frac{1}{2}\,0)$ they describe tilts about [100] of the parent structure, with tilts in successive blocks in the same direction. In our case (with order parameter (a, b) to give a model of *Pmmn* symmetry) there are unequal tilts about both [100] and [010] of the parent structure, and this distortion breaks sufficient symmetry elements to also allow M_3^+ rotations about the long axis (hence the large energy stabilisation calculated for this model from DFT, see Fig. 6). These complex models involving multiple tilts are unusual, but are consistent with the large unit cells reported for $CsCa_2Nb_3O_{10}$ and $RbCa_2Nb_3O_{10}$.[18,48] Being able to describe the structures in terms of symmetry adapted distortions helps explain these complex models.

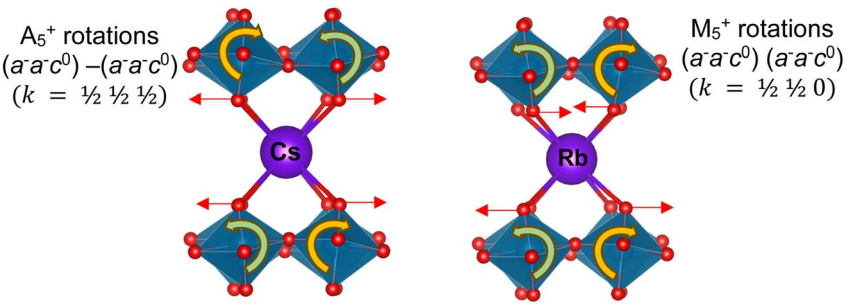

Fig. 8 Figure illustrating (left) A_5^+ rotations of $B(2)O_6$ octahedra and (right) M_5^+ rotations of $B(2)O_6$ octahedra with $B(2)O_6$ octahedra in blue, Cs/Rb ions and oxide ions in purple and red; cooperative rotations of octahedra are shown by curly arrows and resulting oxide displacements by straight red arrows.

To summarise our findings of rotations of BO_6 octahedra in the $n = 3$ Dion–Jacobson series, slight underbonding of A^{2+} cations is relieved by rotations about the long axis (*e.g.*, M_3^+, A_3^+ tilts), but the extent of these tilts is limited by the size of the A'^+ cation (Rb^+, Cs^+): smaller A^{2+} ions will therefore induce additional tilts about in-plane axes. Again the A' size also determines the nature of these tilts: for these odd-layer DJ phases, tilts described by $k = (x\ y\ 0)$ ($k = (x\ y\ \frac{1}{2})$) modes give antiparallel (parallel) displacements of apical O(4) ions immediately above and below the A'^+ cations and so smaller A'^+ cations favour tilts described by $k = (x\ y\ 0)$ modes.

Much of the recent work on Dion–Jacobson phases is motivated by their optoelectronic and catalytic activity[1–6,8,11] and hence understanding their band gaps and edge positions is critical. The optical band gap increases with decreasing A^{2+} size (Fig. 5 and ref. 5, 26, 49 and 53), even though electronic structure calculations have shown that A^{2+} orbitals make negligible contribution to the density of states around the valence band maximum (VBM) and conduction band minimum (CBM).[1] We've shown that decreasing the A^{2+} cation size increases the BO_6 rotations, reducing the *B*–O–*B* angles from 180°. Computational studies (assuming the ideal *P*4/*mmm* structure) have shown that the VBM/CBM are predominantly composed of hybridised *B* 4d/5d and O 2p orbitals.[1,50] This hybridisation is likely to be reduced as *B*–O–*B* bond angles deviate from 180°, giving more narrow bands and wider band gaps.

Optoelectronic effects such as catalytic activity[1] and the photovoltaic effect[54] are also reported to be influenced by polarity in the crystal structure. On one hand, the *B* cation environment may be polar *e.g.*, the *B*(2) cations may be displaced from the centre of the BO_6 octahedra along the long axis towards the A' layers, lowering the *B*(2) site symmetry from Oh or D_{4h} to C_{4v}. Our experimental and computational results do not indicate any clear trend in the magnitude of this displacement across the compositions studied.

It is also important to consider any overall polarity in the crystal structure. It is difficult to confirm the loss of inversion symmetry from powder diffraction data[55] (particularly for these DJ systems which often have quite subtle polar distortions) and SHG measurements (Section 3.1) are extremely valuable for exploring this aspect of the structure and symmetry.[56] Our experimental and computational studies (ESI†) suggest inversion-symmetry-breaking polar distortions of similar magnitudes for $CsCa_2Nb_3O_{10}$ and $RbCa_2Nb_3O_{10}$. The stronger SHG intensity measured for $CsCa_2Nb_3O_{10}$ than for the Rb analogue may reflect need to optimise the particle size for the Rb-containing sample, or the greater hyperpolarizability of Cs–O bonds compared with Rb–O bonds.[57]

Comparison of the $CsCa_2Nb_3O_{10}$ and $CsCa_2Ta_3O_{10}$ models and properties is more tricky: the much reduced orthorhombic distortion for $CsCa_2Ta_3O_{10}$ compared with the Nb analogue leads to greater uncertainty in the experimentally refined models, and to explore the role the B^{5+} ions, comparison between the DFT models might be more reliable. The magnitude of M_3^+ and A_5^+ tilts (about out-of-plane and in-plane axes, respectively) are similar for both Nb^{5+} and Ta^{5+} phases, but the magnitude of the X_3^+ tilts (also about an in-plane axis) and the polar Γ_5^- displacement are noticeably smaller for the Ta^{5+} phase. It should be noted that tilts about in-plane axes (*e.g.* A_5^+ and X_3^+ tilts here, or M_5^+ tilts) and Γ_5^- displacements are not coupled by symmetry (as observed for some tilts in hybrid-improper ferroelectric systems),[13] and yet the magnitude of these distortions appear to be somewhat correlated in our models. Given the almost identical ionic radii of Nb^{5+} and Ta^{5+},[46] any differences between these two phases suggests the role of electronic factors, and in particular, the weaker second-order Jahn–Teller effect for $5d^0$ Ta^{5+} ion.[58]

The non-polar *Pmcn* models (X_3^+ ($+M_3^+$) + A_5^+) allow antipolar in-plane displacements (described by Z_5^+ irreps)[24] *e.g.*, anti-polar displacements of *B*(2) ions along the A_5^+ tilt axis, and our DFT geometry-optimised *Pmcn* models for $CaCa_2B_3O_{10}$ phases have very similar magnitude antipolar distortions (for the overall structures, and for *B*(2) ions specifically) for both phases, perhaps reflecting the very similar geometric effects for B = Nb, Ta phases. There is little difference in magnitude of the anti-polar Z_5^+ distortion for the two compositions in the geometry-optimised polar $P2_1cn$ and $P2_1mn$ models, but the additional in-plane polar displacement gives a small energy gain for $CsCa_2Nb_3O_{10}$, and the magnitude of the displacement is small but non-zero for B = Nb. On the other hand, for B = Ta the polar displacement and the energy gain are both negligible. This polar mode perhaps reflects the additional electronic driving force for lower symmetry (often polar) coordination environments for nd^0 cations due to the second-order Jahn–Teller effect, known to be stronger for Nb^{5+} than for Ta^{5+}.[58] The degree of orthorhombic strain seems to be correlated with the strength of this in-plane polar distortion (Fig. 7). The fact that a non-zero SHG activity is measured for $CsCa_2Ta_3O_{10}$ (Section 3.1) highlights the sensitivity of this technique and likely indicates very subtle polar distortions (associated with only tiny energy gains, see ESI†) that our powder diffraction techniques (which probe the average structure over long length scales) are barely sensitive to.

It is interesting to consider the relative energies of the various structural distortions discussed above. The energy gains for tilts of BO_6 octahedra are always greater than the energies of polar distortions (Fig. 6) for these $A'A_2B_3O_{10}$ (A = Ca, Sr, Ba) phases, as observed for $A = Ln$ (lanthanide) phases.[20] The energies of these non-polar distortions are also similar to those calculated for the proper ferroelectric $CsBi_2Ti_2NbO_{10}$; the key difference is that for $CsBi_2Ti_2NbO_{10}$, containing the second-order Jahn–Teller Bi^{3+} cation, polar and antipolar distortions give much larger energy gains driven by this electronic effect.[59] It should be noted that for the $A'A_2B_3O_{10}$ (A = Ca, Sr, Ba) phases considered here, any polar nature does not arise from hybrid-improper mechanisms[60] (the non-polar tilts described above do not couple to break inversion symmetry), and although the energies associated with polar distortions in $A'Ca_2Nb_3O_{10}$ (A' = Rb, Cs) are small, polarity must arise by proper mechanisms. The difference between $CsCa_2Nb_3O_{10}$ and $CsCa_2Ta_3O_{10}$ (which must have very similar geometric factors) demonstrates the extent of electronic driving forces to stabilise polar structures in these A = Ca, Sr, Ba phases – significantly reduced compared with the role Bi^{3+} plays in $CsBi_2Ti_2NbO_{10}$ compared with the

$CsLn_2Ti_2NbO_{10}$ phases,[20,59] and consistent with work on related $A'Cd_2Nb_3O_{10}$ phases.[44]

5. Conclusions

Our experimental approach, using second-harmonic generation measurements and neutron powder diffraction, combined with DFT calculations, reveals the range of structural distortions observed for $n = 3$ DJ phases and allows us to determine the crystal structures and symmetries for several phases. This study shows how the structure is determined by composition: with decreasing size of A^{2+} cations, BO_6 octahedra first tilt about the out-of-plane axis, and then tilt about an in-plane axis, in order to optimise the bonding environment around increasingly small A^{2+} cations. Larger $A' = Cs$ cations allow tilts about the in-plane axis to be out-of-phase from block to block, but the repulsion between apical oxide sites means that for smaller $A' =$ Rb phases, the tilts about the in-plane axis are in-phase from block to block (Fig. 7). These tilt distortions are largely driven by geometric factors. Previous work has highlighted the electronic role of certain A cations (*e.g.* Bi^{3+}, Cd^{2+}) in stabilising polar phases,[44,59] and our comparison here of $B =$ Nb, Ta analogues indicates that the second-order Jahn–Teller effect involving nd^0 B cations can also play a role (albeit weaker than for ns^2 cations) in stabilising polar DJ phases for the more distorted structures $RbCa_2Nb_3O_{10}$ and $CsCa_2Nb_3O_{10}$. It would be interesting to apply these insights from purely inorganic systems to the hybrid and halide Dion–Jacobson phases,[9,16,61] taking into account the additional bonding influences of the molecular cations.[62]

Data availability

The data supporting this article have been included as part of the ESI† as appropriate. Neutron powder diffraction data are available as "Public Experiments" at **https://tardis.nbi.ansto.gov.au**. Crystallographic data for $CsBa_2Nb_3O_{10}$, $CsSr_2Nb_3O_{10}$, $RbSr_2Nb_3O_{10}$, $CsCa_2Nb_3O_{10}$, $RbCa_2Nb_3O_{10}$ and $CsCa_2Ta_3O_{10}$ will be deposited at the ICSD on acceptance of the manuscript for publication.

Conflicts of interest

There are no conflicts of interest to declare.

Acknowledgements

We thank The Leverhulme Trust (RPG-2017-362) for funding. We are grateful to the Royal Society of equipment grant RG130844 and for international exchange scheme IES\R3\170112, and to the EU Cost Action "Towards oxide-based electronics". We thank the RSC for research fund (R23-4339620653) for equipment for SHG measurements and Warwick seedcorn funding (EP/V007688/1) for supporting preliminary SHG measurements. We acknowledge Durham University for use of their supercomputer services, Hamilton. We are grateful to ANSTO for NPD data. We thank E. Bousquet (Liège) and S. Halasyamani (Houston) for interesting and helpful discussions.

References

1 E. Zahedi, M. Hojamberdiev and M. F. Bekheet, Electronic, optical and photocatalytic properties of three-layer perovskite Dion–Jacobson phase CsBa2M3O10 (M = Ta, Nb): a DFT study, *RSC Adv.*, 2015, **5**(108), 88725–88735, DOI: **10.1039/C5RA13763B**.

2 T. Oshima, T. Yokoi, M. Eguchi and K. Maeda, Synthesis and photocatalytic activity of $K_2CaNaNb_3O_{10}$, a new Ruddlesden–Popper phase layered perovskite, *Dalton Trans.*, 2017, **46**(32), 10594–10601, DOI: **10.1039/C6DT04872B**.

3 S. A. Kurnosenko, O. I. Silyukov, I. A. Rodionov, Y. P. Biryukov, A. A. Burov and I. A. Zvereva, Synthesis, ion-exchange and photocatalytic properties of layered perovskite-like niobate $CsBa_2Nb_3O_{10}$: comparative analysis with related Dion–Jacobson phases $AA'_2Nb_3O_{10}$ (A = K, Rb, Cs; A' = Ca, Sr, Pb), *Russ. J. Inorg. Chem.*, 2023, **68**(13), 1903–1912, DOI: **10.1134/S0036023623602842**.

4 J. R. Reddy, S. Kurra, R. Guje, S. Palla, N. K. Veldurthi, G. Ravi and M. Vithal, Photocatalytic degradation of methylene blue on nitrogen doped layered perovskites, $CsM_2Nb_3O_{10}$ (M = Ba and Sr), *Ceram. Int.*, 2015, **41**(2, Part B), 2869–2875, DOI: **10.1016/j.ceramint.2014.10.109**.

5 O. V. Krasheninnikova, E. V. Syrov, S. M. Smirnov, E. V. Suleimanov, D. G. Fukina, A. V. Knyazev and D. N. Titaev, Synthesis, crystal structure and photocatalytic activity of new Dion–Jacobson type titanoniobates, *J. Solid State Chem.*, 2022, **315**, 123445, DOI: **10.1016/j.jssc.2022.123445**.

6 M. Machida, T. Mitsuyama, K. Ikeue, S. Matsushima and M. Arai, Photocatalytic property and electronic structure of triple-layered perovskite tantalates, $MCa_2Ta_3O_{10}$ (M = Cs, Na, H, and $C_6H_{13}NH_3$), *J. Phys. Chem. B*, 2005, **109**(16), 7801–7806, DOI: **10.1021/jp044833d**.

7 (*a*) H. Ye, Y. Peng, X. Shang, L. Li, Y. Yao, X. Zhang, T. Zhu, X. Liu, X. Chen and J. Luo, Self-powered visible-infrared polarization photodetection driven by ferroelectric photovoltaic effect in a Dion–Jacobson hybrid perovskite, *Adv. Funct. Mater.*, 2022, **32**(24), 2200223, DOI: **10.1002/adfm.202200223**; (*b*) L. Wu, G. Li, K. Prashanthan, A. Musiienko, J. Li, T. W. Gries, H. Zhang, H. Köbler, P. Janasik, A. N. S. Appiah, *et al.*, Stabilization of inorganic perovskite solar cells with a 2D Dion–Jacobson passivating layer, *Adv. Mater.*, 2023, **35**(42), 2304150, DOI: **10.1002/adma.202304150**.

8 M. R. Aziza, C. W. Chang, A. Mohapatra, C. W. Chu, C. C. Kaun and Y. H. Su, Dion–Jacobson phase perovskite $Ca_2Na_{n-3}NbnO_{3n+1}$ (n = 4–6) nanosheets as high-κ photovoltaic electrode materials in a solar water-splitting cell, *ACS Appl. Nano Mater.*, 2020, **3**(7), 6367–6375, DOI: **10.1021/acsanm.0c00747**.

9 H. Fu, Dion–Jacobson halide perovskites for photovoltaic and photodetection applications, *J. Mater. Chem. C*, 2021, **9**(20), 6378–6394, DOI: **10.1039/D1TC01061A**.

10 (*a*) W. Guo, H. Xu, Q. Fan, P. Zhu, Y. Ma, Y. Liu, X. Zeng, J. Luo and Z. Sun, Centimeter-size single crystal of a polar Dion–Jacobson double perovskite with large mobility-lifetime product toward effective X-ray detection, *Adv. Opt. Mater.*, 2024, **12**(17), 2303291, DOI: 10.1002/adom.202303291; (*b*) Q. Fan, Y. Ma, H. Xu, Y. Liu, B. Wang, W. Guo, X. Hu, J. Luo and Z. Sun, Acquiring a newly tailored 2D Dion–Jacobson hybrid perovskite with large structural distortion for efficient crystal array photodetector, *Adv. Opt. Mater.*, 2023, **11**(2), 2202277, DOI: 10.1002/adom.202202277; (*c*) P. Wang, X. Li, H. Ye, Q. Guan, Y. Wang, Y. Geng, C. Zhang, H. Li and J. Luo, Durable dielectric switching and photo-responsivity in a Dion–Jacobson hybrid perovskite semiconductor, *Inorg. Chem. Front.*, 2024, **11**(8), 2436–2441, DOI: 10.1039/D3QI02685J.

11 X. Liu, S. Li, Z. Li, Y. Zhang, W. Yang, Z. Li, H. Liu, D. V. Shtansky and X. Fang, Boosted responsivity and tunable spectral response in B-site substituted 2D Ca_2Nb_3–TaO_{10} perovskite photodetectors, *Adv. Funct. Mater.*, 2021, **31**(20), 2101480, DOI: 10.1002/adfm.202101480.

12 (*a*) W. R. Zhang, K. Fujii, E. Niwa, M. Hagihala, T. Kamiyama and M. Yashima, Oxide-ion conduction in the Dion–Jacobson phase $CsBi_2Ti_2NbO_{10}$, *Nat. Commun.*, 2020, **11**(1), 1224, DOI: 10.1038/s41467-020-15043-z; (*b*) W. R. Zhang, K. Fujii, T. Ishiyama, H. Kandabashi and M. Yashima, Dion–Jacobson-type oxide-ion conductor $CsLa_2Ti_2NbO_{10}$ without phase transitions, *J. Mater. Chem. A*, 2020, **8**(47), 25085–25093, DOI: 10.1039/d0ta06135b.

13 N. A. Benedek, Origin of ferroelectricity in a family of polar oxides: the Dion—Jacobson phases, *Inorg. Chem.*, 2014, **53**(7), 3769–3777, DOI: 10.1021/ic500106a.

14 (*a*) C. Chen, H. P. Ning, S. Lepadatu, M. Cain, H. X. Yan and M. J. Reece, Ferroelectricity in Dion–Jacobson $ABiNb(_2)O(_7)$ (A = Rb, Cs) compounds, *J. Mater. Chem. C*, 2015, **3**(1), 19–22, DOI: 10.1039/c4tc02136c; (*b*) S. Pal, R. Nagarajan and S. Uma, Second harmonic generation in the polar A′SmNb2O7 (A′ = Rb, Cs) Dion–Jacobson layered perovskites, *Chem. Mater.*, 2023, **35**(3), 1249–1258, DOI: 10.1021/acs.chemmater.2c03280.

15 Z.-T. Lu, S. Asaki, S. Yoshida, C. Moriyoshi, G. Hasegawa, K. Fujita, V. Gopalan, K. Hayashi and H. Akamatsu, Structural frustration effects by mixed alkali ions in ferroelectric Dion–Jacobson layered perovskites (Cs,Rb) $NdNb_2O_7$, *J. Mater. Chem. C*, 2025, **13**(4), 1812–1823, DOI: 10.1039/D4TC04190A.

16 L. Mao, W. Ke, L. Pedesseau, Y. Wu, C. Katan, J. Even, M. R. Wasielewski, C. C. Stoumpos and M. G. Kanatzidis, Hybrid Dion–Jacobson 2D lead iodide perovskites, *J. Am. Chem. Soc.*, 2018, **140**(10), 3775–3783, DOI: 10.1021/jacs.8b00542.

17 M. Dion, M. Ganne and M. Tournoux, Nouvelles familles de phases $MIMII_2Nb_3O_{10}$ a feuillets "perovskites", *Mater. Res. Bull.*, 1981, **16**(11), 1429–1435, DOI: 10.1016/0025-5408(81)90063-5.

18 M. Dion, M. Ganne and M. Tournoux, Structure cristalline de la perovskite feuilletee ferroelastique Cs $Ca_2Nb_3O_{10}$, *Rev. Chim. Miner.*, 1984, **21**, 92–103.

19 (*a*) M. N. H. Liton, M. Roknuzzaman, M. A. Helal, M. Kamruzzaman, A. K. M. F. U. Islam, K. Ostrikov and M. K. R. Khan, Electronic, mechanical, optical and photocatalytic properties of perovskite $RbSr_2Nb_3O_{10}$ compound, *J. Alloys Compd.*, 2021, **867**, 159077, DOI: 10.1016/j.jallcom.2021.159077; (*b*) M. A. Rehman, Z. U. Rehman, M. Usman, A. A. Ifseisi, J. Fatima, M. E. Assal and A. Hamad, The photocatalytic degradation performance of Dion–Jacobson-type layered perovskites $AMCa_2Ta_3O_{10}$ (AM = Rb, Cs): a DFT study, *J. Solid State Chem.*, 2024, **337**, 124809, DOI: 10.1016/j.jssc.2024.124809.

20 V. A. Cascos, J. Roberts-Watts, C. Skingle, I. Levin, W. Zhang, P. S. Halasyamani, M. C. Stennett, N. C. Hyatt, E. Bousquet and E. E. McCabe, Tuning between proper and hybrid-improper mechanisms for polar behavior in $CsLn_2Ti_2NbO_{10}$ Dion–Jacobson phases, *Chem. Mater.*, 2020, **32**(19), 8700–8712, DOI: 10.1021/acs.chemmater.0c03326.

21 K. S. Aleksandrov, Structural phase transitions in layered perovskite-like crystals, *Kristallographia*, 1995, **40**, 279–301.

22 T. Zhu, A. S. Gibbs, N. A. Benedek and M. A. Hayward, Complex structural phase transitions of the hybrid improper polar Dion–Jacobson oxides $RbNdM_2O_7$ and $CsNdM_2O_7$ (M = Nb, Ta), *Chem. Mater.*, 2020, **32**(10), 4340–4346, DOI: 10.1021/acs.chemmater.0c01304.

23 M. E. Strayer, A. S. Gupta, H. Akamatsu, S. Lei, N. A. Benedek, V. Gopalan and T. E. Mallouk, Emergent noncentrosymmetry and piezoelectricity driven by oxygen octahedral rotations in n = 2 Dion–Jacobson phase layer perovskites, *Adv. Funct. Mater.*, 2016, **26**(12), 1930–1937, DOI: 10.1002/adfm.201504046.

24 H. T. Stokes, D. M. Hatch and B. J. Campbell, *ISODISTORT, ISOTROPY Software Suite*, http://iso.byu.edu.

25 V. M. Goldschmidt, Die gesetze der krystallochemie, *Naturwissenschaften*, 1926, **14**(21), 477–485, DOI: 10.1007/BF01507527.

26 E. V. Syrov, O. V. Krasheninnikova, A. V. Knyazev, D. G. Fukina, E. V. Suleimanov, N. S. Volkova, A. P. Gorshkov and S. M. Smirnov, Synthesis, structure, and properties of new Dion–Jacobson compounds $A'LnNaNb_3O_{10}$ (A′ = Cs, Rb, H; Ln = Nd, Pr), *J. Phys. Chem. Solids*, 2021, **156**, 110184, DOI: 10.1016/j.jpcs.2021.110184.

27 M. Avdeev and J. R. Hester, ECHIDNA: a decade of high-resolution neutron powder diffraction at OPAL, *J. Appl. Crystallogr.*, 2018, **51**(6), 1597–1604, DOI: 10.1107/S1600576718014048.

28 H. Rietveld, A profile refinement method for nuclear and magnetic structures, *J. Appl. Crystallogr.*, 1969, **2**(2), 65–71, DOI: 10.1107/S0021889869006558.

29 (*a*) TOPAS Academic, *General Profile and Structure Analysis Software for Powder Diffraction Data*, Bruker AXS, Karlsruhe, Germany, 2012; (*b*) A. Coelho, TOPAS and TOPAS-Academic: an optimization program integrating computer algebra and crystallographic objects written in C++, *J. Appl.*

Crystallogr., 2018, **51**(1), 210–218, DOI: 10.1107/S1600576718000183.

30 H. T. Stokes, D. M. Hatch, B. J. Campbell and D. E. Tanner, ISODISPLACE: a web-based tool for exploring structural distortions, *J. Appl. Crystallogr.*, 2006, **39**(4), 607–614, DOI: 10.1107/S0021889806014075.

31 G. Kortüm, W. Braun and G. Herzog, Principles and techniques of diffuse-reflectance spectroscopy, *Angew. Chem., Int. Ed. Engl.*, 1963, **2**(7), 333–341, DOI: 10.1002/anie.196303331.

32 S. K. Kurtz and T. T. Perry, A powder technique for the evaluation of nonlinear optical materials, *J. Appl. Phys.*, 1968, **39**(8), 3798–3813, DOI: 10.1063/1.1656857.

33 (*a*) S. J. Clark, M. D. Segall, C. J. Pickard, P. J. Hasnip, M. I. J. Probert, K. Refson and M. C. Payne, First principles methods using CASTEP, *Z. Kristallogr., Cryst. Mater.*, 2005, **220**(5–6), 567–570, DOI: 10.1524/zkri.220.5.567.65075; (*b*) M. D. Segall, J. D. L. Philip, M. J. Probert, C. J. Pickard, P. J. Hasnip, S. J. Clark and M. C. Payne, First-principles simulation: ideas, illustrations and the CASTEP code, *J. Phys.: Condens. Matter*, 2002, **14**(11), 2717, DOI: 10.1088/0953-8984/14/11/301.

34 J. P. Perdew, K. Burke and M. Ernzerhof, Generalized gradient approximation made simple, *Phys. Rev. Lett.*, 1996, **77**(18), 3865–3868, DOI: 10.1103/PhysRevLett.77.3865.

35 D. Vanderbilt, Soft self-consistent pseudopotentials in a generalized eigenvalue formalism, *Phys. Rev. B: Condens. Matter Mater. Phys.*, 1990, **41**(11), 7892–7895, DOI: 10.1103/PhysRevB.41.7892.

36 J. D. García, F. Gómez, V. Velázquez and B. A. Rodríguez, Bulk second-order optical nonlinearities in centrosymmetric materials, *J. Opt. Soc. Am. B*, 2022, **39**(10), 2582–2588, DOI: 10.1364/JOSAB.466210.

37 J. I. Dadap, J. Shan and T. F. Heinz, Theory of optical second-harmonic generation from a sphere of centrosymmetric material: small-particle limit, *J. Opt. Soc. Am. B*, 2004, **21**(7), 1328–1347, DOI: 10.1364/JOSAB.21.001328.

38 T. Wu, B. Yin, Z. Bian, Y. Gao, J. Gu and D. Wang, Insights into the mechanism of the symmetry dependent SHG properties in low dimensional $KNbO_3$ structures, *Inorg. Chem. Front.*, 2023, **10**(9), 2689–2696, DOI: 10.1039/D2QI02691K.

39 M. Hojamberdiev, M. F. Bekheet, E. Zahedi, H. Wagata, Y. Kamei, K. Yubuta, A. Gurlo, N. Matsushita, K. Domen and K. Teshima, New Dion–Jacobson phase three-layer perovskite $CsBa_2Ta_3O_{10}$ and its conversion to nitrided $Ba_2Ta_3O_{10}$ nanosheets *via* a nitridation–protonation–intercalation–exfoliation route for water splitting, *Cryst. Growth Des.*, 2016, **16**(4), 2302–2308, DOI: 10.1021/acs.cgd.6b00081.

40 Z.-H. Liang, K.-B. Tang, Q.-W. Chen and H.-G. Zheng, $RbCa_2Nb_3O_{10}$ from X-ray powder data, *Acta Crystallogr., Sect. E*, 2009, **65**(6), i44, DOI: 10.1107/S1600536809018157.

41 V. Thangadurai, P. Schmid-Beurmann and W. Weppner, Synthesis, structure, and electrical conductivity of A′ [A2B3O10](A′ = Rb, Cs; A = Sr, Ba; B = Nb, Ta): new members of Dion–Jacobson-type layered perovskites, *J. Solid State Chem.*, 2001, **158**(2), 279–289, DOI: 10.1006/jssc.2001.9108.

42 K. Toda, T. Teranishi, Z.-G. Ye, M. Sato and Y. Hinatsu, Structural chemistry of new ion-exchangeable tantalates with layered perovskite structure: new Dion–Jacobson phase $MCa_2Ta_3O_{10}$ (M = alkali metal) and ruddlesden–popper phase $Na_2Ca_2Ta_3O_{10}$, *Mater. Res. Bull.*, 1999, **34**(6), 971–982, DOI: 10.1016/S0025-5408(99)00084-7.

43 X. Wang, J. Adhikari and L. J. Smith, An investigation of distortions of the Dion–Jacobson phase $RbSr_2Nb_3O_{10}$ and its acid-exchanged form with 93Nb solid state NMR and DFT calculations, *J. Phys. Chem. C*, 2009, **113**(40), 17548–17559, DOI: 10.1021/jp902318v.

44 S. Atri, M. Pokhriyal and S. Uma, Synergistic Influence of d0 (Nb_5^+) and d10 (Cd_2^+) cations in stabilizing noncentrosymmetric Dion–Jacobson layered perovskites, $A'Cd_2Nb_3O_{10}$ (A′ = Rb, Cs), *Inorg. Chem.*, 2020, **59**(12), 8044–8053, DOI: 10.1021/acs.inorgchem.0c00291.

45 S. Pal, S. Das, R. Nagarajan and S. Uma, Dion–Jacobson A′MiiiNaNb$_3$O$_{10}$ (A′ = Rb, Cs; M(iii) = Sm, Bi) and $RbSmNa_2Nb_4O_{13}$ layered perovskites and their luminescent function, *J. Mater. Chem. C*, 2022, **10**(39), 14675–14685, DOI: 10.1039/D2TC03179E.

46 R. D. Shannon, Revised effective ionic-radii and systematic studies of interatomic distances in halides and chalcogenides, *Acta Crystallogr., Sect. A*, 1976, **32**(SEP1), 751–767, DOI: 10.1107/s0567739476001551.

47 (*a*) A. J. Tuxworth, E. E. McCabe, D. G. Free, S. J. Clark and J. S. O. Evans, Structural characterization and physical properties of the new transition metal oxyselenide $La_2O_2ZnSe_2$, *Inorg. Chem.*, 2013, **52**(4), 2078–2085, DOI: 10.1021/ic302484x; (*b*) H. Djani, E. E. McCabe, W. Zhang, P. S. Halasyamani, A. Feteira, J. Bieder, E. Bousquet and P. Ghosez, $Bi_2W_2O_9$: a potentially antiferroelectric aurivillius phase, *Phys. Rev. B*, 2020, **101**(13), 134113, DOI: 10.1103/PhysRevB.101.134113; (*c*) E. A. S. Scott, E. Mitoudi Vagourdi, M. Johnsson, V. Cascos, F. John, D. Pickup, A. V. Chadwick, H. Djani, E. Bousquet, W. Zhang, *et al.*, Bi2CoO$_2$F$_4$–A polar, ferrimagnetic aurivillius oxide-fluoride, *Chem. Mater.*, 2022, **34**(21), 9775–9785, DOI: 10.1021/acs.chemmater.2c02745.

48 J. A. Kurzman and M. J. Geselbracht, Probing octahedral tilting in Dion–Jacobson layered perovskites with neutron powderdiffraction and Raman spectroscopy, *MRS Proc.*, 2007, **988**, 9880806.

49 Y.-m. Ding, J.-j. Shi, M. Zhang, M. Wu, H. Wang, Y.-l. Cen, W.-h. Guo and S.-h. Pan, Electronic, photocatalytic and piezoelectric properties of n = 3 Dion–Jacobson-type perovskite monolayer A′[$A_2B_3O_{10}$], *Mater. Res. Express*, 2018, **5**(9), 096305, DOI: 10.1088/2053-1591/aad892.

50 I. E. Castelli, K. S. Thygesen and K. W. Jacobsen, Calculated optical absorption of different perovskite phases, *J. Mater. Chem. A*, 2015, **3**(23), 12343–12349, DOI: 10.1039/C5TA01586C.

51 N. C. Hyatt, I. M. Reaney and K. S. Knight, Ferroelectric-paraelectric phase transition in the $n = 2$ Aurivillius phase $Bi_3Ti_{1.5}W_{0.5}O_9$: a neutron powder diffraction study,

Phys. Rev. B: Condens. Matter Mater. Phys., 2005, **71**(2), 024119, DOI: **10.1103/PhysRevB.71.024119**.

52 V. Yadav, S. Pal and S. Uma, Dion–Jacobson (n = 2) layered perovskites ($A'SmTa_2O_7$; A′ = Rb, Cs) as potential ferroelectric materials, *J. Phys. Chem. C*, 2025, **129**(11), 5666–5673, DOI: **10.1021/acs.jpcc.4c08181**.

53 S. Hussain, J. U. Rehman, M. B. Tahir and A. Hussain, First principles calculations of double perovskite $RbX_2Y_3O_{10}$ (X = Ca, Ba: YCd, Ta) materials for photocatalytic applications, *Int. J. Hydrogen Energy*, 2024, **89**, 486–495, DOI: **10.1016/j.ijhydene.2024.09.355**.

54 D. Fu, Y. Ma, C.-Y. Su, Z. Chen and D.-W. Fu, Amplification of polarization ratio is observed in monolayer Dion–Jacobson hybrid perovskites, *J. Mater. Chem. C*, 2023, **11**(34), 11492–11499, DOI: **10.1039/D3TC01926H**.

55 IUCr, *Friedel's Law*, 2021, **https://dictionary.iucr.org/Friedel%27s_law**, accessed 2021.

56 K. M. Ok, E. O. Chi and P. S. Halasyamani, Bulk characterization methods for non-centrosymmetric materials: second-harmonic generation, piezoelectricity, pyroelectricity, and ferroelectricity, *Chem. Soc. Rev.*, 2006, **35**(8), 710–717, DOI: **10.1039/B511119F**.

57 (*a*) S. H. Patil and K. T. Tang, A simple method for polarizabilities and hyperpolarizabilities of alkali isoelectronic systems, *Chem. Phys. Lett.*, 1998, **295**(1), 152–157, DOI: **10.1016/S0009-2614(98)00917-8**; (*b*) A. Alejo-Molina, H. Hardhienata and K. Hingerl, Simplified bond-hyperpolarizability model of second harmonic generation, group theory, and Neumann's principle, *J. Opt. Soc. Am. B*, 2014, **31**(3), 526–533, DOI: **10.1364/JOSAB.31.000526**.

58 P. M. Woodward; P. Karen; J. S. O. Evans and T. Vogt, *Solid State Materials Chemistry*, Cambridge University Press, 2021.

59 E. E. McCabe, E. Bousquet, C. P. J. Stockdale, C. A. Deacon, T. T. Tran, P. S. Halasyamani, M. C. Stennett and N. C. Hyatt, Proper ferroelectricity in the Dion–Jacobson material $CsBi_2Ti_2NbO_{10}$: experiment and theory, *Chem. Mater.*, 2015, **27**(24), 8298–8309, DOI: **10.1021/acs.chemmater.5b03564**.

60 E. Bousquet, M. Dawber, N. Stucki, C. Lichtensteiger, P. Hermet, S. Gariglio, J. M. Triscone and P. Ghosez, Improper ferroelectricity in perovskite oxide artificial superlattices, *Nature*, 2008, **452**(7188), 732–U734, DOI: **10.1038/nature06817**.

61 J. Gong, M. Hao, Y. Zhang, M. Liu and Y. Zhou, Layered 2D halide perovskites beyond the Ruddlesden–Popper phase: tailored interlayer chemistries for high-performance solar cells, *Angew. Chem., Int. Ed.*, 2022, **61**(10), e202112022, DOI: **10.1002/anie.202112022**.

62 T. Liu, N. P. Holzapfel and P. M. Woodward, Understanding structural distortions in hybrid layered perovskites with the $n = 1$ Ruddlesden-Popper structure, *IUCrJ*, 2023, **10**(4), 385–396, DOI: **10.1107/S2052252523003743**.

